Nano Energy 77 (2020) 105188

Contents lists available at ScienceDirect

Nano Energy

journal homepage: http://www.elsevier.com/locate/nanoen

Enhanced long-term cyclability in Li-Rich layered oxides by electrochemically constructing a $Li_xTM_{3-x}O_4$-type spinel shell

Mingjian Zhang [a,b,1], Zhibo Li [a,1], Lei Yu [c], Defei Kong [a], Yiwei Li [a], Bo Cao [a], Wenguang Zhao [a], Jianguo Wen [c,**], Feng Pan [a,*]

[a] School of Advanced Materials, Peking University, Shenzhen Graduate School, Shenzhen, 518055, People's Republic of China
[b] Center for Advanced Radiation Source (ChemMatCARS), The University of Chicago, Lemont, IL, 60439, United States
[c] Center for Nanoscale Materials, Argonne National Laboratory, Lemont, IL, 60439, United States

ARTICLE INFO

Keywords:
Li-ion batteries
Li-rich layered oxides
Cycling stability
$Li_xTM_{3-x}O_4$-type spinel shell
Structural degradation

ABSTRACT

The poor long-term cycling stability, including the fast capacity fade and the severe voltage decay, has become the main concern hindering the practical application of Li-rich layered oxides, a promising cathode for high-energy-density Li-ion battery. Herein, we design and electrochemically construct a ~10 nm-thick $Li_xTM_{3-x}O_4$-type (TM = Ni, Co, Mn, $0 < x < 1$) spinel shell at the particle surface, which possesses both the good structural stability of TM_3O_4-type spinel phase and the good Li^+ conductivity of $LiMn_2O_4$-type spinel phase. Systemic structural and electrochemical analysis demonstrate that, it slows down the activation rate of Li_2MnO_3 component and efficiently alleviates the lattice O loss at high voltage (>4.5 V) and Mn dissolution, thereby suppressing the structural degradation from the layered phase to the spinel phase in the bulk, eventually significantly enhancing the long-term cycling stability. This study adds richness into the Mn-based spinel phase system and provides a new heterostructure design strategy to improve the electrochemical performance of Li-rich layered cathodes and beyond.

1. Introduction

Since Li-rich layered oxide cathode materials were first introduced by Dahn and Thackeray [1,2], they have attracted much attention due to the high specific capacities (>250 mA h g^{-1}), thus becoming promising candidates to meet the requirements of high-energy-density Li-ion batteries for electric vehicles and grid-scale storage. Nevertheless, these materials still encounter some problems: (1) the large irreversible capacity loss during the 1st cycle, namely the low initial Coulombic efficiency at the 1st cycle compared to other cathode materials, usually below 80% [3]; (2) the poor rate performance, a decrease of the capacity by around 30% at 1C than that at 0.1C [4]; (3) the poor cycling stability, including a fast capacity fading and discharge voltage decay during cycling [5,6]. These issues lead to a reduced energy density as well as an increased difficulty in judging the state of charge in batteries, thus greatly hindering their commercial use.

In general, Li-rich layered oxide is considered to be composed of a $LiTMO_2$ (TM = Ni, Co, Mn) component with rhombohedral *R*-3*m* structure and a Li_2MnO_3 component with monoclinic *C*2/*m* structure [5,7–9], and the formula is typically written as $xLiTMO_2 \cdot (1\text{-}x)Li_2MnO_3$. The former component contributes to the electrochemistry mainly through TM redox below 4.5 V, while the later through the oxygen redox above 4.5 V [10]. The oxygen redox above 4.5 V, accompanying with the simultaneous Li^+ de/intercalation from the Li_2MnO_3 component, is usually called the activation process of Li_2MnO_3 component, which plays an essential role in providing superior capacity of Li-rich layered cathodes [11,12]. Unfortunately, it brings with the irreversible lattice O loss in the form of O_2 as well as subsequent TM migration to Li layers and results in the irreversible phase transition from the layered phase to the spinel phase, namely the serious structural degradation, which is identified as the main cause for the poor cycling stability [13–16]. This structural degradation is considered to be closely related with the activation process of Li_2MnO_3 component, and the accelerated activation of Li_2MnO_3 component has been demonstrated to result in a faster

* Corresponding author.
** Corresponding author.
E-mail addresses: jwen@anl.gov (J. Wen), panfeng@pkusz.edu.cn (F. Pan).
[1] These authors contribute equally to the work.

https://doi.org/10.1016/j.nanoen.2020.105188
Received 6 March 2020; Received in revised form 17 June 2020; Accepted 8 July 2020
Available online 26 July 2020

structural degradation, leading to a rapid capacity decrease [17].

To solve this problem, many strategies have been adopted during the synthesis, such as lattice/surface doping with Zr, Zn, Nb, Na, Mg, B, etc. [18–23], surface coating with Li_3VO_4, $Li_2O{\cdot}2B_2O_3$, graphene, Nb_2O_5, etc. [24–27], and special architecture design, such as introducing spinel-like structure at the particle surface through an acid treatment process [28], and creating a hollow spherical structure by co-precipitation [29,30]. Thereinto, design of core-shell heterostructure has become one efficient route. In consideration of 3D lithium diffusion channels in spinel structures and the same cubic close-packed oxygen arrays with layered phase, various layered-spinel core-shell heterostructures have been constructed by post-synthesis coating or chemical oxidation processing [31–36], which demonstrates the enhanced cyclability and rate capability. Two spinel phases, $LiMn_2O_4$-type and $Li_4Mn_5O_{12}$-type with Mn^{3+}/Mn^{4+} and Mn^{4+}, are commonly-used ones. Nevertheless, the studies into $LiMn_2O_4$ and $Li_4Mn_5O_{12}$ also exhibit the irreversible structural degradation and not good enough electrochemical stability due to Jahn-Teller-distortion induced anisotropic strain, Mn dissolution, the poor thermal stability and etc. [37–40] Therefore, searching for new electrochemical stable spinel phases is essential for further performance improvement.

Herein, we design and electrochemically construct a unique core-shell heterostructure with a $Li_xTM_{3-x}O_4$-type spinel thin shell in a representative Li-rich layered oxide $Li_{1.2}Ni_{0.13}Co_{0.13}Mn_{0.54}O_2$ ($0.5LiNi_{1/3}Co_{1/3}Mn_{1/3}O_2{\cdot}0.5Li_2MnO_3$, denoted as LMO114). Various techniques, including high resolution transmission electron microscopy (HRTEM), electron energy loss spectroscopy (EELS), and X-ray diffraction (XRD), and etc., are employed to characterize this new spinel phase, revealing the good structural stability with low valent Mn (+2/+3) and the excellent mechanical integration with the native layered phase. It effectively alleviates the lattice O loss and Mn dissolution, suppresses the irreversible structural degradation in the bulk, and eventually significantly enhances the long-term cycling stability. These findings further enrich the knowledge into Mn-based spinel phase system, and provide more heterostructure design strategies to solve the cycling stability issue of Li-rich layered oxides and beyond.

2. Results and discussions

2.1. Design of layered-spinel core-shell heterostructure

As shown in Scheme 1, there are three types of Mn-based spinel phases known so far, i.e. $Li_4Mn_5O_{12}$, $LiMn_2O_4$, and TM_3O_4 (Co_3O_4-type). The Mn valences in these spinel phases decrease from +4 to +3/+4 to +2/+3 associated with the reduction of Li content in the framework, respectively. As depicted, there is Li^+/Mn^{4+} co-occupancy in the octahedral sites and Li^+ fully occupancy in the tetrahedral sites for $Li_4Mn_5O_{12}$-type spinel phase, which evolves to 100% Mn occupancy in the octahedral sites with low valent $Mn^{3+/4+}$ for $LiMn_2O_4$-type spinel phase. With further decreasing of Mn valence to +2/+3, the tetrahedra sites occupied by Li^+ in $Li_4Mn_5O_{12}$ and $LiMn_2O_4$, are replaced by $Mn^{2+/3+}$ in TM_3O_4-type spinel phase. Due to the stronger covalent binding in Mn–O bond than the ionic binding in Li–O bond, TM_3O_4-type spinel phase manifests the best structural stability among the three spinel phases. However, the poor Li^+ conductivity is expected in TM_3O_4-type spinel phase owing to full occupation of Mn ions at both octahedral and tetrahedral sites. If octahedral sites are fully occupied by TM cations and the tetrahedral sites are co-occupied by Li/Mn cations, this phase would be able to provide both good structural stability and Li^+ conductivity. From the structural viewpoint, this $Li_xMn_{3-x}O_4$-type spinel phase is an

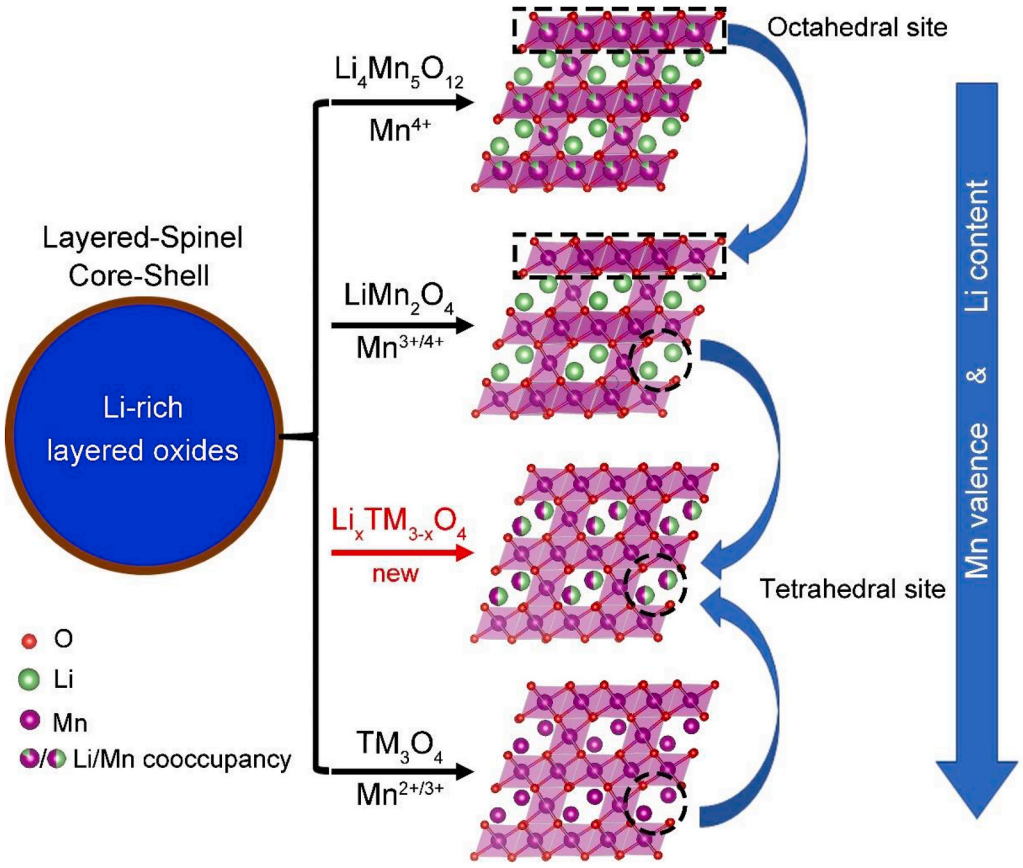

Scheme 1. Design of layered-spinel core-shell structure to solve the concern of the structural/electrochemical degradation in Li-rich layered oxides. The crystal structures for three known kinds of spinel phases ($Li_4Mn_5O_{12}$-type, $LiMn_2O_4$-type, and TM_3O_4-type (TM = Mn/Co/Ni)) and one new spinel phase $Li_xTM_{3-x}O_4$-type, are compared above.

intermediate phase between TM_3O_4-type and $LiMn_2O_4$-type.

To implement such design, we utilize a general principle in the electrochemical cycling: the charge/discharge (delithiation/lithiation) extent decreases from the particle surface to the bulk. The closer to the particle surface, the larger charge/discharge extent. By carefully adjusting the upper cut-off voltage to 4.5 V, a key point between TM redox reaction and O redox reaction, the particle surface may be able to cycle at the deep charge/discharge states, while the bulk can cycle in the shadow charge/discharge states. With such an approach, it is expected to construct a stable spinel phase at the particle surface and maintain a layered phase in the bulk [41]. In a typical process, LMO114 with the spherical secondary particle morphology (Fig. S1) was prepared as a representative Li-rich layered oxide. The voltage range was set 2.5–4.5 V under a current density of 50 mA g^{-1} (0.2C) in the first 5 cycles to fast degrade the layered phase to the spinel phase at the particle surface, and then go back to the normal cycling (2.5–4.8 V at 1C) from the 6th cycle. The charge/discharge profiles for the first 5 activated cycles are shown in Fig. S2, and these cells are labelled as activated cells. In comparison, the normal charge/discharge in the potential range of 2.5–4.8 V on the same batch of electrodes are performed. These cells are labelled as normal cells. It is worth mentioning that, we tried different activation cycles and compared the cycling performance at 1C (Fig. S3), finally determining to use 5 cycles as the activation cycles.

2.2. Construction of the new spinel shell at the primary particle surface

XRD pattern and the corresponding Rietveld refinement are carried out to investigate the crystal structure of as-prepared LMO114, shown in

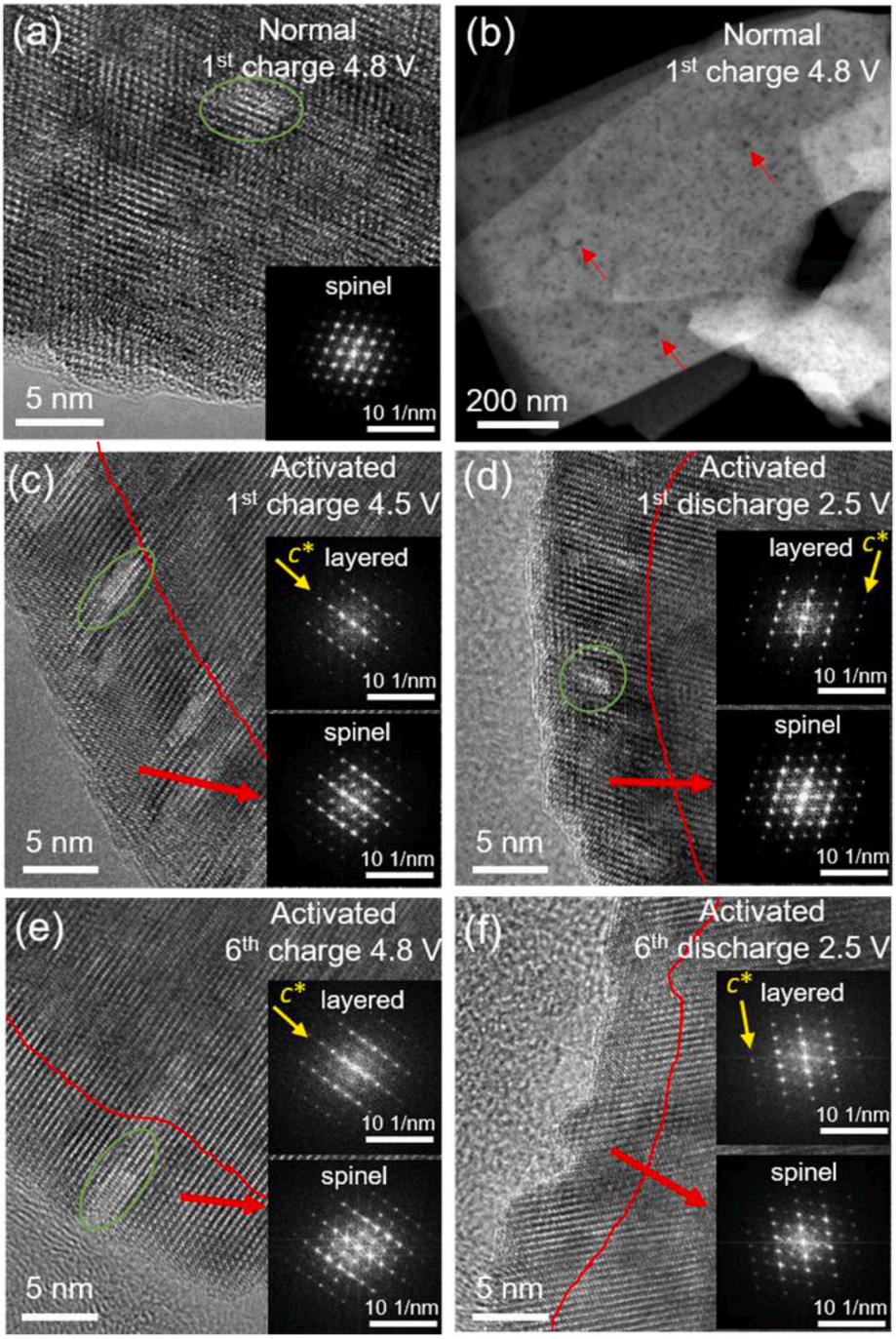

Fig. 1. Local structural analysis to demonstrate the construction of a unique $Li_xTM_{3-x}O_4$-type spinel shell at the particle surface. HRTEM image as well as the corresponding FFT pattern (a) and HADDF image (b) of the normal electrode when charged to 4.8 V at the 1st cycle. HRTEM images of the activated electrodes when charged to 4.5 V (c) and discharged back to 2.5 V (d) at the 1st activation cycle and the selected-area FFT patterns. HRTEM images of the activated electrodes when charged to 4.8 V (e) and discharged back to 2.5 V (f) at the 6th cycle and the selected-area FFT patterns. The red lines in c-f are used to distinguish the surface and bulk regions, which correspond to the spinel phase and the layered phase, respectively. The green curves in a and c-e are used to mark the possible oxygen voids in the surface region.

Fig. S4a. The refined parameters are deposited in Table S1. All peaks except for those weak peaks between 20 and 25°, can be indexed as a typical α-$NaFeO_2$ type layered structure (space group *R*-3*m*). The peaks between 20 and 25°, marked by a dashed wine rectangle, are the superstructure peaks, which come from a Li_2MnO_3-type monoclinic phase (space group *C*2/*m*) [42–44]. HRTEM image of as-prepared LMO114 is shown in Fig. S4b. Well-defined lattice fringes can be indexed to (003) crystallographic planes in the typical layered structure, and the inset, Fast Fourie Transform (FFT) pattern further confirms the well-ordered layered structure [45,46].

To examine the local structural changes at the particle surface induced by the charge/discharge strategy designed above, HRTEM coupling with FFT patterns were also performed for activated cells and normal cells. In the normal charge/discharge strategy, the irreversible phase transition leads to the formation of $LiMn_2O_4$-type spinel phase [13–16], which is confirmed by the charge valence of Mn discussed in the EELS part as below. As shown in Fig. 1a, the FFT pattern of the whole image is obviously different from the FFT pattern derived from the pristine layered phase (Fig. S4b). Extra reflection lines in between the original reflection lines correspond to a typical phase transformation to a spinel phase, representing the Mn migration from TM layers to Li layers. It indicates the formation of a >40-nm-thick spinel shell when directly charging to 4.8 V during the 1st cycle. In addition, the bright contrasted region (marked by the green circle in Fig. 1a) is observed in bright-field TEM image, collaborated by the dark contrasted regions spreading over the entire primary particle in HAADF image (Fig. 1b), which confirm the formation of lots of oxygen voids [47]. These oxygen voids can be attributed to the serious lattice oxygen loss at high voltages. When discharged back to 2.5 V at the 1st cycle (Fig. S4c), the spinel phase in the shell cannot be recovered back to the layered phase, demonstrating the irreversibility of the phase transition. That is the critical reason for the poor cycling stability of Li-rich layered oxides.

In contrast, a new spinel shell is constructed when initially charging to 4.5 V in the activated electrode. As shown in Fig. 1c, the FFT pattern derived from the near-surface region (marked by the red line) is similar with that in Fig. S4, hinting that, a thin spinel shell with the thickness of ~10 nm is formed at the particle surface of the activated electrode when initially charging to 4.5 V. Some bright contrasted regions marked by green circles mainly locate in the thin spinel shell, which can be also assigned to the oxygen voids. There is no clear structural transition boundary between the spinel shell and the layered bulk, demonstrating an excellent mechanical integration in this core-shell heterostructure. In addition, more TEM images with higher magnification (Fig. S5) show that, the continuous spinel phase formed at the particle surface, hinting the good uniformity of the spinel shell. After the 1st discharge, the thin spinel shell is found no further propagation into the bulk in Fig. 1d, showing the good structural stability. Fig. 1e–f shows HRTEM images of the shell after charging the activated electrodes to 4.8 V and discharging back to 2.5 V during the 1st normal cycle (the 6th cycle), respectively. The spinel shell still maintains the thickness of around 10–15 nm, in comparison with that in Fig. 1c-d. Notably, the bright region marked by the green curve becomes bigger in Fig. 1e, and even links up together in Fig. 1f, indicating the formation of a uniform spinel shell at the particle surface.

2.3. Local chemical analysis in the spinel shell

As mentioned above, the most important difference between three types of spinel phases is the Mn valence. To identify the types of the spinel phases formed in activated electrodes and normal electrodes, scanning transmission electron microscopy (STEM)-EELS is adopted to compare the chemical difference in the electrode samples charged to 4.5 V (activated) and 4.8 V (normal), respectively.

Fig. 2 presents the HADDF images and the corresponding line-scan EELS spectra. First, there is a visible contrast nonuniformity in the HADDF image of the normal electrode (Fig. 2a), in comparison with that of activated electrode (Fig. 2b). Since these HAADF images are acquired using a high cut-off angle, the HAADF image is an atomic number (Z)-contrast image and its intensity is approximately proportional to Z^2. These areas with dark contrast in Fig. 2a correspond to white contrast areas in bright-field TEM images in Fig. 1a, resulting from oxygen voids in the thick spinel shell of the normal electrode [48–50]. O–*K* and Mn-$L_{2,3}$ EELS spectra are stacked in Fig. 2c–f from the particle surface to the bulk along the yellow arrows in Fig. 2a and b. On the whole, the shapes of O–*K* edge (Fig. 2c) and Mn-*L* edge (Fig. 2e) keep nearly unchanged from the surface to the bulk for the normal electrode, and the pre-peak of O–*K* edge is much lower than the main peak of O–*K* edge, indicating a uniform and relatively low charge valence of Mn at the particle surface, which is consistent with the thick spinel shell in Fig. S4c. In contrast, the pre-peak of O–*K* edge obviously intensifies from the surface to the particle for the activated cell, marked by the blue dotted ellipse in Fig. 2d, indicating a higher Mn valence in the bulk as compared to the surface [50]. This result is further confirmed by a significant blue shift of Mn-L_3 peak from the surface to the bulk (Fig. 2f), which corresponds to the phase transition from the spinel phase to the layered phase observed in Fig. 1c.

The peak positions and the ratio of peak intensity (denoted as L_3/L_2 ratio) of Mn-$L_{2,3}$ edges are very sensitive to Mn valence [37]. A close examination of Mn valence variation from surface to bulk is performed for the activated and normal samples. As shown in Fig. 2g and h, the positions of Mn-L_3 and Mn-L_2 peaks, and L_3/L_2 ratio are plotted as functions of the distance from the surface. Both the positions of Mn-L_3 and Mn-L_2 peaks and L_3/L_2 ratio are kept constant from the surface to a 40-nm depth, confirming the chemical uniformity in the thick spinel shell for the normal electrode. Differently, the curves in Fig. 2h show a distinct 2-step stage at around 10 nm, which corresponds to the core-shell structure with 10 nm-thick spinel phase at the surface. The larger L_3/L_2 ratio in the range of 0–10 nm than that in the range of 10–45 nm indicates a lower valence of Mn in the thin spinel shell than that in the bulk with layered phase. Viewing along the three vertical grey lines, it is surprising to observe that, the positions of Mn-L_3 and Mn-L_2 peaks, and L_3/L_2 ratio for the normal electrode lie in between the corresponding curves for the activated electrode. It indicates that, the valence state of Mn in the thick spinel shell of electrode charged to 4.8 V is higher than that in the thin spinel shell of electrode charged to 4.5 V, and both of them are lower than that in the bulk. Combining the local chemical difference of Mn/O with the structural degradation mechanism in Li_2MnO_3 [41], we can deduce that, the structure of the thick spinel shell should be a Li/O-deficient $LiMn_2O_4$-type spinel phase (with Mn^{4+}/Mn^{3+}), and the structure of the thin spinel shell may be a $Li_xMn_{3-x}O_4$-type (x~0–1) spinel phase (with Mn^{3+}/Mn^{2+}).

In addition, ICP was used to characterize the composition change in activated and normal electrodes after 6 cycles. As shown in Table S2, Ni, Co and Mn contents were normalized by the content of Co. Mn and Ni content (3.93 and 0.66) in activated electrode are both higher than those in normal electrode (3.60 and 0.63), indicating that, the spinel shell can efficiently inhibit the Mn and Ni dissolution in the electrolyte. It should be beneficial to maintain the structural stability during cycling.

2.4. Enhanced long-term cyclability

To examine the effect of the $Li_xTM_{3-x}O_4$-type spinel shell on the electrochemical performance, systemic comparison was performed between activated cells and normal cells. The charge/discharge curves at different cycles for normal and activated cells are first examined. As shown in Fig. 3a, the normal cell shows a very long plateau at around 4.55 V during the 1st charge (the black curve), taking about 2/3 of the charge capacity, which corresponds to the oxygen redox in a typical Li-rich layered oxide [51]. The large irreversible capacity (120 mA h g^{-1}) leads to a very low initial coulombic efficiency (62.7%), which is consistent with the previous reports (≤80%) [3]. With the increasing cycle number, the discharge capacity as well as the medium voltage

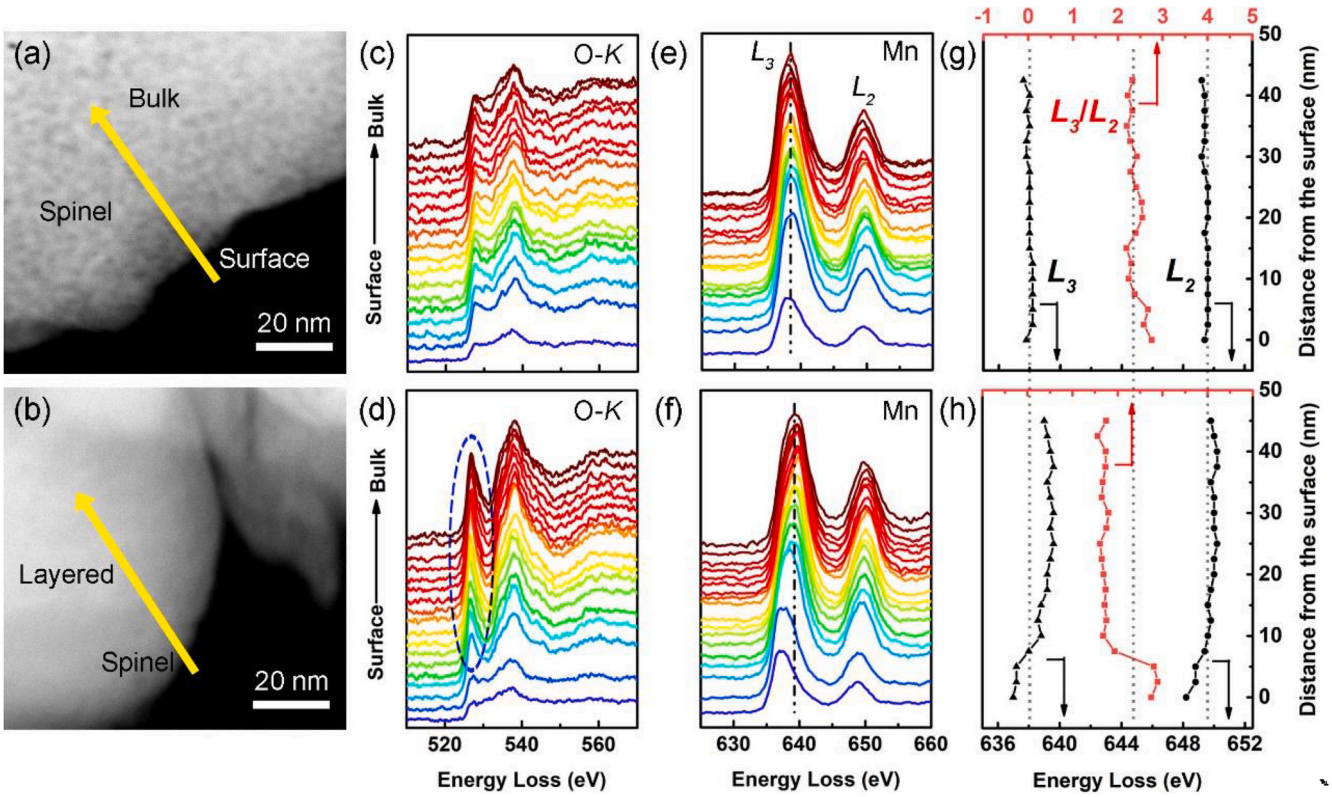

Fig. 2. Local chemical analysis into the spinel shell electrochemically constructed. HADDF images of the normal electrode (a) and the activated electrode (b). EELS profiles of O–*K* (c), (d) and Mn-$L_{2,3}$ edges (e), (f) recorded from the surface to the bulk along the red arrows in the corresponding HADDF images (the inset) for the normal electrode (a) and the activated electrode (b). The black dotted lines mark the positions of Mn-L_3 peaks for the normal electrode and the activated electrode. Peak positions of Mn-L_3 and Mn-L_2 peaks, and L_3/L_2 ratio as functions of the distance from the surface for the normal electrode (g) and activated electrode (h) The grey lines mark the positions of the Mn-L_3 and Mn-L_2 peaks, and L_3/L_2 ratio for the normal electrode.

(shown in Fig. S7) decrease very fast. For the activated cell, the plateau at 4.55 V only contributes less than half to the charge capacity during the 1st cycle (the black curve) in Fig. 3b, which indicates much less contribution from oxygen redox after activation, and brings with a relatively high coulombic efficiency (82.9%). The corresponding dQ/dV curves are also compared in Fig. S8. Since Peak R2 and Peak R3 peak correspond to the reduction of Mn^{4+}/Mn^{3+} in the layered phase and the $LiMn_2O_4$-like spinel phase, respectively [28], suppressed structural degradation from layered phase to spinel phase are clearly demonstrated by the slew-down change speed from R2 reduction to R3 reduction peak in the activated cell.

The cycling performance of normal and activated cells (after activation) at 1C are displayed in Fig. 3c. Interestingly, the specific capacity of activated cell gradually increases during the initial 15 cycles (marked by the red ellipse), which can be attributed to the gradual electrochemical activation of Li_2MnO_3 component [12,17,52,53], and should be closely related with the oxygen redox reaction above 4.5 V. The specific capacity goes up to the highest value of 211.73 mA h g^{-1} at the 15th cycle. In contrast, the normal cell has a relatively low specific capacity of 182.25 mA h g^{-1} at the 1st cycle. After 200 cycles, the discharge capacity and capacity retention for the activated cell are 159.64 mA h g^{-1} and 74.64%, respectively, which is much superior to the normal cell (109.45 mA h g^{-1} and 60.05%) and most of the previous reports (Fig. S9) [54–58]. In order to validate the reliability of the result, another two cells are assembled and tested, giving the similar result in Fig. S10. Fig. 3d shows the rate performance of the normal cell and the activated cell. The charge/discharge rate is increased from 0.2C to 5C stepwise and finally returned to 0.2C. The activated cell displays a more prominent rate capability, 240, 214, 186, 152, 104 mA h g^{-1} at 0.2, 0.5, 1, 2 and 5C, respectively. In comparison, the discharge capacities of the normal cell are low, 215, 198, 173, 141 and 96 mA h g^{-1} at 0.2, 0.5, 1, 2 and 5C, respectively. In addition, the capacity of the activated cell can return to 234 mA h g^{-1} at 0.2C after 25 cycles at high rates, which indicates that, the activated cell not only has excellent capacities but also owns outstanding cycling stability even at high rate. In addition, Li^+ diffusion coefficients for both cells before cycling and after the 6th cycle were measured by the cyclic voltammograms (CV) method (Fig. S11 and Table S3), indicating enhanced Li^+ diffusivity by the unique spinel shell. Fig. 3e show the cycling performance for both cells at high rate of 5C. The capacity retention of activated cell is nearly 100% after 350 cycles, superior than that of normal cell (51.17%). It further confirms the enhanced cycling stability by the $Li_xTM_{3-x}O_4$-type spinel shell. The similar capacities at 5C in the initial cycles for both cells can be ascribed to the larger polarization by the unique spinel shell, which is revealed in the corresponding charge/discharge curves in Fig. S12. In one word, the construction of $Li_xTM_{3-x}O_4$-type spinel shell enables both higher specific capacity and much improved cycling stability for Li-rich layered oxides than the normal cycling strategy. The structural stability of this spinel phase was also checked after 100 cycles. As shown in Fig. S13b, the initial spinel shell surprisingly transforms to a rock-salt phase with the similar thickness (~10 nm) after 100 cycles, which possesses the denser atomic stacking and can provide better protection for the layered phase in the bulk.

2.5. *Mechanism analysis for the enhanced long-term cyclability*

Based on the systemic local structural/chemical analysis above, a reasonable hypothesis is proposed here to explain the mechanism of the suppressed structural degradation and the enhanced cycling stability. As illustrated in Fig. 4, the entire process can be divided into two parts: i) *in-situ* construction of the $Li_xMn_{3-x}O_4$-type spinel shell in Fig. 4a; ii) the impact of the spinel shell on the structure and electrochemistry in

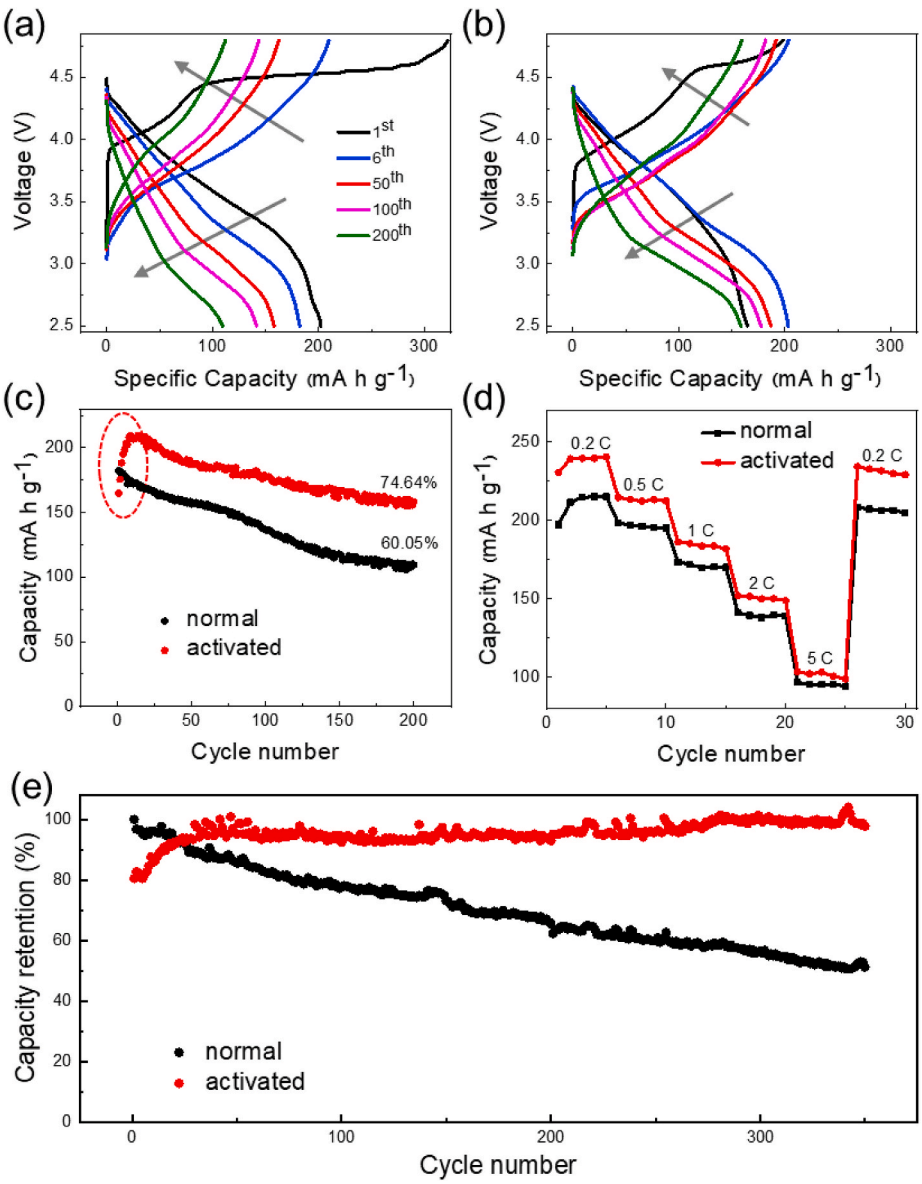

Fig. 3. Enhanced cycling stability by the $Li_xMn_{3-x}O_4$-type spinel shell. (a) Charge/discharge curves of the normal cell in the 1st, 6th, 50th, 100th and 200th cycles at 25 °C and 1C (1C = 250 mA g^{-1}). (b) Charge/discharge curves of the activated cell in the 1st, 6th, 50th, 100th and 200th normal cycles (after activation) at 25 °C and 1C. The grey arrows indicate the change trend of the curves. (c) The cycling performance of the normal and activated cells at 25 °C and 1C. (d) The rate performance of the normal and activated cells. (e) The cycling performance of the normal and activated cells at 25 °C and 5C.

Fig. 4b.

As shown in Fig. 4a, the initial structure within primary particle is a typical layered phase with Mn^{4+}. During normal cycling using high cutoff potential 4.8 V, TM redox and oxygen redox occur at the particle surface in a deep extent, which greatly weakens metal-oxygen bonds, resulting into a flexible oxygen framework. Both oxygen loss and TM dissolution probably happen, inducing TM migration to Li layers to form a thick $LiMn_2O_4$-type defect spinel shell with reduced Mn^{3+}/Mn^{4+}. When cycled at low cutoff potential 4.5 V, TM redox dominates in the bulk of the particle, and make the bulk still preserve the layered phase. Considering that the extent of the electrochemical reaction gradually becomes weak from the surface to the bulk, oxygen redox may occur in the near-surface region of the primary particle in the meanwhile, accelerating the structural degradation and resulting into a thin $Li_xMn_{3-x}O_4$-type defect spinel shell with Li/Mn mixing in tetrahedral sites. It is electrochemically stable and much denser than $LiMn_2O_4$-type spinel phase due to Li/TM co-occupancy. Therefore, this dense and stable spinel shell can greatly suppress oxygen loss and Mn dissolution during the subsequent long-term cycling, and significantly delay the irreversible structural degradation, and exhibit an enhanced cycling stability. In addition, as shown in Fig. 4b, this unique spinel shell was observed to be able to slow down the activation rate of Li_2MnO_3 component, making it gradually activate during the first 15 cycles (Fig. 3c). It should be related with the unique electric property of the spinel phase, and is another reason for the protection role of the spinel shell.

In the previous reports about layered-spinel core-shell heterostructure in Li-rich layered oxides, $Li_4Mn_5O_{12}$-type or $LiMn_2O_4$-type spinel shell was constructed in the synthesis process, *via* the chemical processing by some reductive reagents, including $Na_2S_2O_8$, hydrazine, urea, $(NH_4)_2S_2O_8$, and $NH_3{\cdot}H_2O$), and subsequent calcination [31–35]. Herein, the feasibility of electrochemically constructing a spinel shell is demonstrated, showing the similar effects in improving electrochemical performance. In addition, tuning the charge/discharge strategy to maximize the electrochemical performance actually has been reported [53,59–64]. However, the structural origin beneath the enhanced cyclability has never been clearly understood. $Li_xTM_{3-x}O_4$-type spinel phase observed here provides a kind of reasonable explanation.

3. Conclusions

In summary, we design and electrochemically construct a unique $Li_xMn_{3-x}O_4$-type spinel thin shell with a low valence state of Mn at the

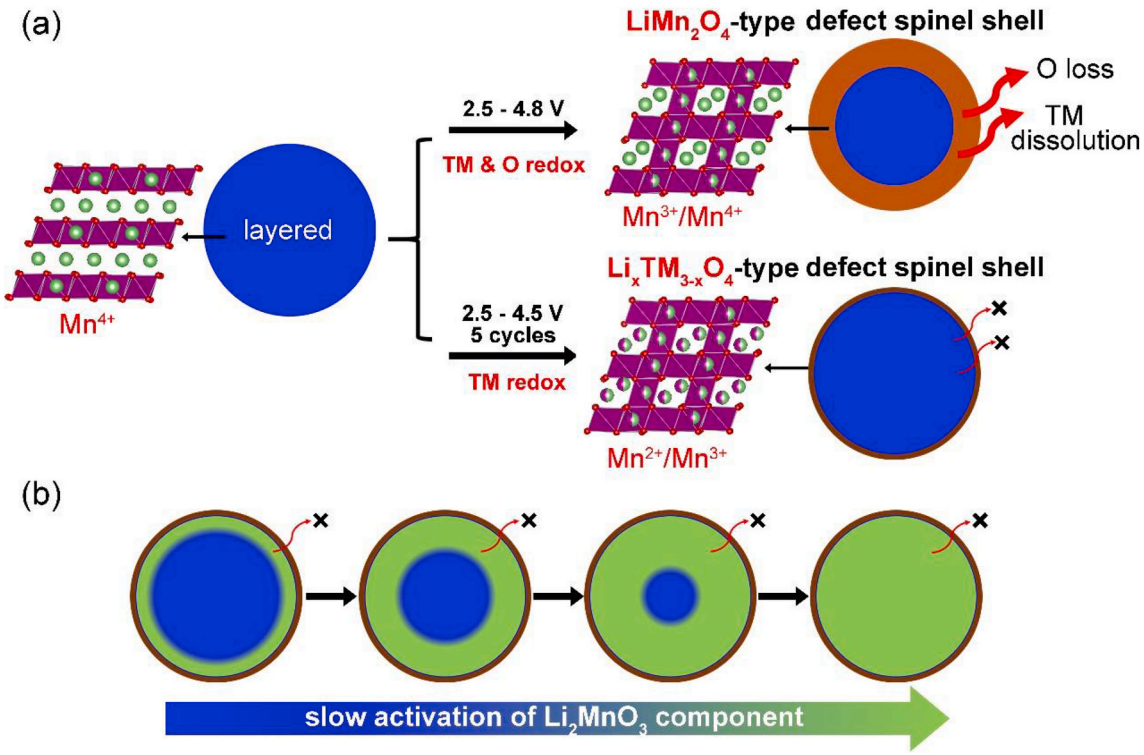

Fig. 4. Scheme illustration to show the electrochemical construction process and the protection role of $Li_xTM_{3-x}O_4$-type spinel shell (0<x<1). (a) The electrochemical construction process of the $Li_xTM_{3-x}O_4$-type spinel shell. (b) The impact of the $Li_xTM_{3-x}O_4$-type spinel shell on the electrochemistry upon the subsequent long-term cycling, including the gradual activation of Li_2MnO_3 component at a low rate, the suppressed lattice oxygen loss and Mn dissolution, and the suppressed structural degradation, thus the improved cycling stability.

particle surface of LMO114. It combines the characters of $LiMn_2O_4$-type and M_3O_4-type spinel phases together, possessing both good structural stability and Li^+ conductivity. Advanced structural and chemical characterization as well as the systemic electrochemical evaluation reveal that, this unique spinel shell slows down the activation of Li_2MnO_3 component and suppresses the oxygen release and TM dissolution in the subsequent cycles at high voltage, thus efficiently reduces the irreversible structural degradation and enhances the long-term cyclability. All these findings enrich the understanding into the Mn-based spinel phase system, and also open a new avenue to optimize the electrochemical performance of Li-rich layered cathodes and beyond, by electrochemically constructing favorable surface structure.

CRediT authorship contribution statement

Mingjian Zhang: Formal analysis, Writing - review & editing, Visualization, Supervision. **Zhibo Li:** Conceptualization, Investigation, Data curation, Writing - original draft, Visualization. **Lei Yu:** Data curation, Visualization. **Defei Kong:** Conceptualization. **Yiwei Li:** Conceptualization, Investigation, Data curation. **Bo Cao:** Investigation, Data curation. **Wenguang Zhao:** Data curation, Visualization. **Jianguo Wen:** Supervision, Writing - review & editing. **Feng Pan:** Supervision, Writing - review & editing, Project administration, Funding acquisition.

Declaration of competing interest

The authors declare that they have no known competing financial interests or personal relationships that could have appeared to influence the work reported in this paper.

Acknowledgments

This work was financially supported by National Key R&D Program of China (2016YFB0700600), Soft Science Research Project of Guangdong Province (No. 2017B030301013), Shenzhen Science and Technology Research Grant (ZDSYS201707281026184). NSF's ChemMatCARS Sector 15 is supported by the Divisions of Chemistry (CHE) and Materials Research (DMR), National Science Foundation, under grant number NSF/CHE-1834750. This work including electron microscopy was performed, in part, at the Center for Nanoscale Materials, a U.S. Department of Energy Office of Science User Facility, and supported by the U.S. Department of Energy, Office of Science, under Contract No. DE-AC02-06CH11357.

Appendix A. Supplementary data

Supplementary data to this article can be found online at https://doi.org/10.1016/j.nanoen.2020.105188.

References

[1] Z.H. Lu, L.Y. Beaulieu, R.A. Donaberger, C.L. Thomas, J.R. Dahn, J. Electrochem. Soc. 149 (2002) A778–A791.
[2] M.M. Thackeray, C.S. Johnson, J.T. Vaughey, N. Li, S.A. Hackney, J. Mater. Chem. 15 (2005) 2257–2267.
[3] R. Shunmugasundaram, R.S. Arumugam, J.R. Dahn, Chem. Mater. 27 (2015) 757–767.
[4] X.Q. Yu, Y.C. Lyu, L. Gu, H.M. Wu, S.M. Bak, Y.N. Zhou, K. Amine, S.N. Ehrlich, H. Li, K.W. Nam, X.Q. Yang, Adv. Energy Mater. 4 (2014) 1300950.
[5] J.M. Zheng, S.J. Myeong, W.R. Cho, P.F. Yan, J. Xiao, C.M. Wang, J. Cho, J. G. Zhang, Adv. Energy Mater. 7 (2017) 1601284.
[6] H.J. Yu, H.S. Zhou, J. Phys. Chem. Lett. 4 (2013) 1268–1280.
[7] J. Hong, H. Gwon, S.K. Jung, K. Ku, K. Kang, J. Electrochem. Soc. 162 (2015) A2447–A2467.
[8] P. Rozier, J.M. Tarascon, J. Electrochem. Soc. 162 (2015) A2490–A2499.
[9] J. Wang, X. He, E. Paillard, N. Laszczynski, J. Li, S. Passerini, Adv. Energy Mater. 6 (2016) 1600906.
[10] Z.H. Lu, J.R. Dahn, J. Electrochem. Soc. 149 (2002) A815–A822.
[11] J.R. Croy, K.G. Gallagher, M. Balasubramanian, B.R. Long, M.M. Thackeray, J. Electrochem. Soc. 161 (2014) A318–A325.

[12] D.L. Ye, G. Zeng, K. Nogita, K. Ozawa, M. Hankel, D.J. Searles, L.Z. Wang, Adv. Funct. Mater. 25 (2015) 7488–7496.
[13] B.H. Song, Z.W. Liu, M.O. Lai, L. Lu, Phys. Chem. Chem. Phys. 14 (2012) 12875–12883.
[14] M. Sathiya, A.M. Abakumov, D. Foix, G. Rousse, K. Ramesha, M. Saubanere, M. L. Doublet, H. Vezin, C.P. Laisa, A.S. Prakash, D. Gonbeau, G. VanTendeloo, J. M. Tarascon, Nat. Mater. 14 (2015) 230–238.
[15] M. Gu, I. Belharouak, J.M. Zheng, H.M. Wu, J. Xiao, A. Genc, K. Amine, S. Thevuthasan, D.R. Baer, J.G. Zhang, N.D. Browning, J. Liu, C.M. Wang, ACS Nano 7 (2013) 760–767.
[16] A. Boulineau, L. Simonin, J.F. Colin, E. Canevet, L. Daniel, S. Patoux, Chem. Mater. 24 (2012) 3558–3566.
[17] L. Xiao, J. Xiao, X.Q. Yu, P.F. Yan, J.M. Zheng, M. Engelhard, P. Bhattacharya, C. M. Wang, X.Q. Yang, J.G. Zhang, Nano Energy 16 (2015) 143–151.
[18] H. Chen, Q.Y. Hu, Z.M. Huang, Z.J. He, Z.X. Wang, H.J. Guo, X.H. Li, Ceram. Int. 42 (2016) 263–269.
[19] J.K. Zhao, Z.X. Wang, H.J. Guo, X.H. Li, Z.J. He, T. Li, Ceram. Int. 41 (2015) 11396–11401.
[20] S. Liu, Z.P. Liu, X. Shen, W.H. Li, Y.R. Gao, M.N. Banis, M.S. Li, K. Chen, L. Zhu, R. C. Yu, Z.X. Wang, X.L. Sun, G. Lu, Q.Y. Kong, X.D. Bai, L.Q. Chen, Adv. Energy Mater. 8 (2018) 1802105.
[21] B. Qiu, J. Wang, Y.G. Xia, Y.Z. Liu, L.F. Qin, X.Y. Yao, Z.P. Liu, J. Power Sources 240 (2013) 530–535.
[22] Z.M. Huang, X.H. Li, Y.H. Liang, Z.J. He, H. Chen, Z.X. Wang, H.J. Guo, Solid State Ionics 282 (2015) 88–94.
[23] L.C. Pan, Y.G. Xia, B. Qiu, H. Zhao, H.C. Guo, K. Jia, Q.W. Gu, Z.P. Liu, J. Power Sources 327 (2016) 273–280.
[24] Q. Fu, F. Du, X.F. Bian, Y.H. Wang, X. Yan, Y.Q. Zhang, K. Zhu, G. Chen, C.Z. Wang, Y.J. Wei, J. Mater. Chem. A 2 (2014) 7555–7562.
[25] M.H. Bai, Z.X. Wang, X.H. Li, H.J. Guo, Z.J. He, J.K. Zhao, Solid State Ionics 292 (2016) 66–69.
[26] J.L. Cheng, X.H. Li, Z.J. He, Z.X. Wang, H.J. Guo, W.J. Peng, Mater. Technol. 31 (2016) 658–665.
[27] W. Pan, W.J. Peng, G.C. Yan, H.J. Guo, Z.X. Wang, X.H. Li, W.H. Gui, J.X. Wang, N. Chen, Energy Technol. Ger. 6 (2018) 2139–2145.
[28] J.R. Croy, D. Kim, M. Balasubramanian, K. Gallagher, S.H. Kang, M.M. Thackeray, J. Electrochem. Soc. 159 (2012) A781–A790.
[29] Z.J. He, Z.X. Wang, Z. Huang, H. Chen, X.H. Li, H.J. Guo, J. Mater. Chem. A 3 (2015) 16817–16823.
[30] Z.J. He, J. Ping, Z.J. Yi, C. Peng, C.S. Shen, J.S. Liu, J. Alloys Compd. 708 (2017) 1038–1045.
[31] C. Yang, Q. Zhang, W.X. Ding, J. Zang, M. Lei, M.S. Zheng, Q.F. Dong, J. Mater. Chem. A 3 (2015) 7554–7559.
[32] S.J. Han, B. Qiu, Z. Wei, Y.G. Xia, Z.P. Liu, J. Power Sources 268 (2014) 683–691.
[33] P. Oh, S. Myeong, W. Cho, M.J. Lee, M. Ko, H.Y. Jeong, J. Cho, Nano Lett. 14 (2014) 5965–5972.
[34] D. Luo, G.S. Li, C.C. Fu, J. Zheng, J.M. Fan, Q. Li, L.P. Li, Adv. Energy Mater. 4 (2014) 1400062.
[35] B. Wu, X.K. Yang, X. Jiang, Y. Zhang, H.B. Shu, P. Gao, L. Liu, X.Y. Wang, Adv. Funct. Mater. 28 (2018) 1803392.
[36] X.D. Zhang, J.L. Shi, J.Y. Liang, Y.X. Yin, J.N. Zhang, X.Q. Yu, Y.G. Guo, Adv. Mater. 30 (2018) 1801751.
[37] T.C. Liu, A. Dai, J. Lu, Y.F. Yuan, Y.G. Xiao, L. Yu, M. Li, J. Gim, L. Ma, J.J. Liu, C. Zhan, L.X. Li, J.X. Zheng, Y. Ren, T.P. Wu, R. Shahbazian-Yassar, J.G. Wen, F. Pan, K. Amine, Nat. Commun. 10 (2019) 4721.
[38] J. Lu, C. Zhan, T.P. Wu, J.G. Wen, Y. Lei, A.J. Kropf, H.M. Wu, D.J. Miller, J. W. Elam, Y.K. Sun, X.P. Qiu, K. Amine, Nat. Commun. 5 (2014) 5693.
[39] L. Jaber-Ansari, K.P. Puntambekar, S. Kim, M. Aykol, L.L. Luo, J.S. Wu, B.D. Myers, H. Iddir, J.T. Russell, S.J. Saldana, R. Kumar, M.M. Thackeray, L.A. Curtiss, V. P. Dravid, C. Wolverton, M.C. Hersam, Adv. Energy Mater. 5 (2015) 1500646.
[40] C. Alie, C. Calberg, C. Paez, D. Liquet, D. Eskenazi, B. Heinrichs, N. Job, J. Power Sources 403 (2018) 173–183.
[41] K. Shimoda, M. Oishi, T. Matsunaga, M. Murakami, K. Yamanaka, H. Arai, Y. Ukyo, Y. Uchimoto, T. Ohta, E. Matsubara, Z. Ogumi, J. Mater. Chem. A 5 (2017) 6695–6707.
[42] M.M. Thackeray, S.H. Kang, C.S. Johnson, J.T. Vaughey, R. Benedek, S.A. Hackney, J. Mater. Chem. 17 (2007) 3112–3125.
[43] J. Breger, M. Jiang, N. Dupre, Y.S. Meng, Y. Shao-Horn, G. Ceder, C.P. Grey, J. Solid State Chem. 178 (2005) 2575–2585.
[44] Z.H. Lu, Z.H. Chen, J.R. Dahn, Chem. Mater. 15 (2003) 3214–3220.
[45] C. Lin, J.Y. Li, C.M. Wang, F. Pan, Chin. J. Struct. Chem. 38 (2019) 2015–2019.
[46] Z. Zheng, M.Y. Weng, L.Y. Yang, Z.X. Hu, Z.F. Chen, F. Pan, Chin. J. Struct. Chem. 38 (2019) 2020–2026.
[47] P.F. Yan, J.M. Zheng, Z.K. Tang, A. Devaraj, G.Y. Chen, K. Amine, J.G. Zhang, L. M. Liu, C.M. Wang, Nat. Nanotechnol. 14 (2019) 602–608.
[48] H. Zhang, B.M. May, F. Omenya, M.S. Whittingham, J. Cabana, G. Zhou, Chem. Mater. 31 (2019) 7790–7798.
[49] A. Nurpeissova, M.H. Choi, J.-S. Kim, S.-T. Myung, S.-S. Kim, Y.-K. Sun, J. Power Sources 299 (2015) 425–433.
[50] P. Yan, J. Zheng, J.G. Zhang, C. Wang, Nano Lett. 17 (2017) 3946–3951.
[51] Y. Sun, H.J. Cong, L. Zang, Y.X. Zhang, ACS Appl. Mater. Interfaces 9 (2017) 38545–38555.
[52] D.L. Ye, B. Wang, Y. Chen, G. Han, Z. Zhang, D. Hulicova-Jurcakova, J. Zou, L. Z. Wang, J. Mater. Chem. A 2 (2014) 18767–18774.
[53] S.H. Yu, T. Yoon, J. Mun, S. Park, Y.S. Kang, J.H. Park, S.M. Oh, Y.E. Sung, J. Mater. Chem. A 1 (2013) 2833–2839.
[54] X. Miao, Y. Yan, C. Wang, L. Cui, J. Fang, G. Yang, J. Power Sources 247 (2014) 219–227.
[55] M. Chen, D. Chen, Y. Liao, X. Zhong, W. Li, Y. Zhang, ACS Appl. Mater. Interfaces 8 (2016) 4575–4584.
[56] Y.-P. Deng, F. Fu, Z.-G. Wu, Z.-W. Yin, T. Zhang, J.-T. Li, L. Huang, S.-G. Sun, J. Mater. Chem. A 4 (2016) 257–263.
[57] J. Li, T. Jia, K. Liu, J. Zhao, J. Chen, C. Cao, J. Power Sources 333 (2016) 37–42.
[58] B. Hu, X. Lou, C. Li, F. Geng, M. Yang, M. Shen, B. Hu, Chemelectrochem 6 (2019) 1385–1392.
[59] A. Ito, D.C. Li, Y. Sato, M. Arao, M. Watanabe, M. Hatano, H. Horie, Y. Ohsawa, J. Power Sources 195 (2010) 567–573.
[60] W.W. Yan, H. Wen, Y.Z. Chen, Y.P. Wang, Y.N. Liu, J. Power Sources 277 (2015) 76–83.
[61] J.S. Yang, L.F. Xiao, W. He, J.W. Fam, Z.X. Chen, X.P. Ai, H.X. Yang, Y.L. Cao, ACS Appl. Mater. Interfaces 8 (2016) 18867–18877.
[62] P.K. Nayak, J. Grinblat, E. Levi, B. Markovsky, D. Aurbach, J. Power Sources 318 (2016) 9–17.
[63] S. Liu, X. Feng, X.L. Wang, X. Shen, E.Y. Hu, R.J. Xiao, R.C. Yu, H.T. Yang, N. N. Song, Z.X. Wang, X.Q. Yang, L.Q. Chen, Adv. Energy Mater. 8 (2018) 1703092.
[64] W.W. Yan, Y.N. Liu, S.K. Chong, Y.F. Wu, RSC Adv. 6 (2016) 23677–23685.